Article

Sliding and healing of frictional interfaces that appear stationary

https://doi.org/10.1038/s41586-025-08673-0

Received: 28 February 2024

Accepted: 17 January 2025

Published online: 12 March 2025

Check for updates

Krittanon Sirorattanakul[1✉], Stacy Larochelle[1,4], Vito Rubino[2,5], Nadia Lapusta[1,3] & Ares J. Rosakis[2]

Frictional interfaces are found in systems ranging from biological joints to earthquake faults. When and how these interfaces slide is a fundamental problem in geosciences and engineering[1–20]. It is believed that there exists a threshold shear force, called static friction, below which the interface is stationary[4,10], despite many studies suggesting that this concept is outdated[1,21–28]. By contrast, rate-and-state friction formulations[1,26,27] predict that interfaces are always sliding[29], but this feature is often considered an artefact that calls for modifications[30]. Here we show that nominally stationary interfaces subjected to constant shear and normal loads, with a driving force that is notably below the classically defined static friction for which creep is known to occur[9,27–29], are sliding, but with diminishingly small rates down to 10^{-12} m s^{-1}. Our precise measurements directly at the interface are enabled by digital image correlation[18,31,32]. This behaviour contradicts classical models of friction but confirms the prediction of rate-and-state friction[1,26,27]. The diminishing slip rates of nominally stationary interfaces reflect interface healing, which would manifest itself in higher peak friction in subsequent slip events[15,27,33], such as earthquakes and landslides, substantially modifying their nucleation and propagation and hence their hazard[3,12,13,34].

Sliding of frictional interfaces[1] is a fundamental problem with numerous engineering and geosciences applications such as earthquakes[2–4], landslides[5], glacier flow[6,7] and vibrations of automobile breaks[8]. The key parameter governing sliding is the ratio of shear to normal force (or stress, defined as force per unit area) on the interface. A common assumption, dating back to Coulomb, Amontons and before[4,9,10], is that a frictional interface in stationary contact remains in stationary contact until the ratio of the shear to normal force reaches a threshold value called the static friction coefficient (f_s). A conventional way to measure the static friction coefficient is by placing an object on an inclined plane and slowly tilting the plane until the object starts to (visibly) slide at some critical inclination angle α_{crit} (Fig. 1a). Consequently, $f_s = \tan \alpha_{crit}$. After sliding is initiated, the ratio of the shear to normal force is governed by the kinetic friction coefficient f_k, which is often lower. In the simplest Coulomb law, the transition from f_s to f_k is instantaneous, which is non-physical[4]. However, it is still widely used today to model landslides, earthquakes and other phenomena[35,36] owing to its simplicity. Slip-weakening laws[37,38] allow the transition from f_s to f_k to occur with slip (Fig. 1b), providing a link to cohesive zone models in fracture mechanics[39]. These friction laws are widely used in modelling earthquake rupture[11,40,41]. Although slip-weakening laws are more realistic than the instantaneous Coulomb law, they lack strengthening mechanisms and therefore cannot be used to model how the interface regains strength before future events, as occurs in earthquake sequences.

More detailed friction measurements show that the friction coefficient $f(t)$ depends on the rate of slip $V(t)$ and has memory effects encoded in an evolving state variable $\theta(t)$, which has led to the development of the empirical rate-and-state friction (RSF) formulations[1,13,21,26,27]. For example,

$$f(t) = f^* + a \ln\left(\frac{V(t)}{V^*}\right) + b \ln\left(\frac{V^*\theta(t)}{D_{RS}}\right) \tag{1}$$

$$\frac{d\theta}{dt} = 1 - \frac{V(t)\theta(t)}{D_{RS}} \tag{2}$$

$$\frac{d\theta}{dt} = -\frac{V(t)\theta(t)}{D_{RS}} \ln\left(\frac{V(t)\theta(t)}{D_{RS}}\right) \tag{3}$$

where t is time, f^* is a reference friction coefficient at reference slip rate V^*, D_{RS} is the critical slip distance and a and b are nondimensional parameters quantifying the direct and evolutionary effects, respectively. Several state evolution laws have been proposed, including the ageing and slip ones given in equations (2) and (3), respectively. Equation (1) is undefined when slip rate $V = 0$ because log(0) is undefined. Therefore, based on an Arrhenius-activated rate process describing creep at asperity contacts, equation (1) is often regularized by replacing the logarithmic function of slip rate V with a function that makes

[1]Seismological Laboratory, Division of Geological and Planetary Sciences, California Institute of Technology, Pasadena, CA, USA. [2]Graduate Aerospace Laboratories, California Institute of Technology, Pasadena, CA, USA. [3]Mechanical and Civil Engineering, Division of Engineering and Applied Science, California Institute of Technology, Pasadena, CA, USA. [4]Present address: Lamont-Doherty Earth Observatory, Columbia University, Palisades, NY, USA. [5]Present address: Nantes Université, École Centrale Nantes, CNRS, Institut de Recherche en Génie Civil et Mécanique (GeM), Nantes, France. ✉e-mail: krittanon.pond@gmail.com

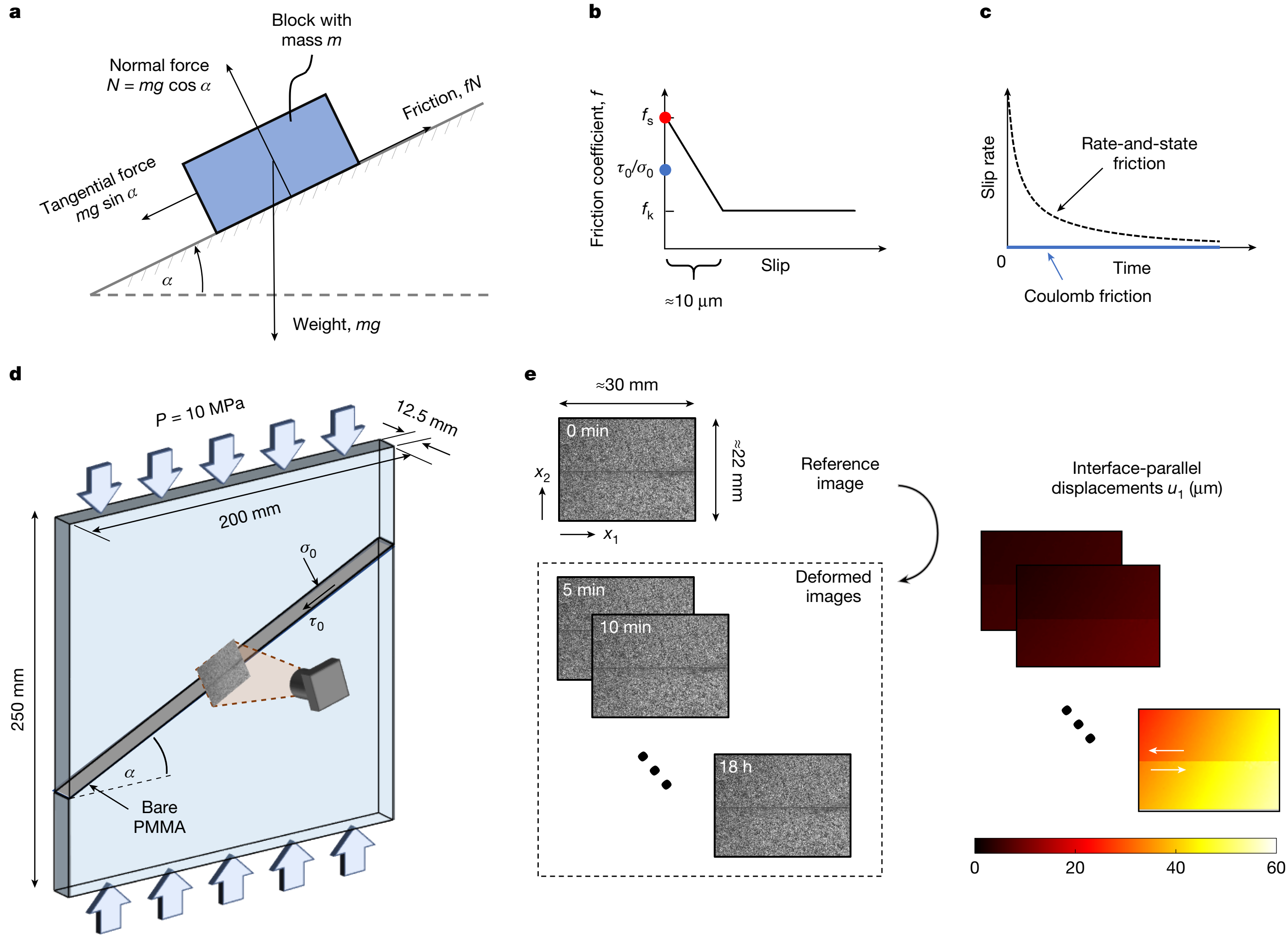

Fig. 1 | Testing the concept of static friction. a, A block on an inclined plane. The notion of static friction posits that the block should remain motionless for inclination angles α below the critical value given by $\tan\alpha_{crit} = f_s$. **b**, Slip-weakening friction law. According to this widely used classical model, the ratio of shear to normal stresses (τ_0/σ_0) needs to reach a critical value (f_s) for sliding to start. As sliding proceeds, the friction coefficient transitions from the static value f_s to a lower kinetic value f_k over some slip. **c**, Schematic slip rate evolution for a nominally stationary interface governed by experimentally derived RSF laws that predict that frictional interfaces under shear stress always slide. **d**, Experimental setup designed to study frictional PMMA interfaces with inclination angles below α_{crit} and hence $\tau_0/\sigma_0 < f_s$. A digital camera continuously monitors the displacements of a portion of the interface. The load is maintained for 18 h in most experiments and 2 weeks in one experiment. Optical images are taken every 5 min. **e**, The full-field distribution of displacements and hence slip across the interface is measured by DIC.

the zero slip rate only possible for zero shear stress[12,13,42] (Methods). The rate-and-state formulation has proven successful in explaining several time-dependent behaviours of the earthquake source, such as the evolution of postseismic slip and aftershock rates after the mainshock[2,14,43], presence of both locked and slowly creeping segments on natural faults[44,45], correlation of earthquakes with periodic loading such as solid Earth tides and hydromechanical variations[22], slow-slip driven earthquake swarms[23] and induced seismicity[24].

One of the predictions of the rate-and-state framework is that all interfaces under nonzero shear stress are sliding with nonzero slip rates, in contrast to the concept of static friction[29] (Fig. 1c). Another prediction is that the interface heals at low enough slip rates, with the healing manifesting itself through higher peak friction during subsequent rapid sliding episodes, as observed in slide–hold–slide experiments[15,27,33]. The exact nature of sliding during the hold times has profound implications for healing and how it should be incorporated into the friction laws[15,27,28,33]. However, sliding has rarely been directly measured at the interface during hold portions in previous experiments[19,27], but rather inferred through measurements of the load-point displacement and applied load, which additionally requires an estimate of the stiffness of the experimental apparatus[16,33]. Furthermore, the physics during holds is not well understood and could differ from what is described by the rate-and-state framework (equations (1)–(3)), for example, that the slip rate vanishes at a threshold, as assumed by some modelers[30]. Here we perform local optical measurements of sliding during nominal holds with constant shear and normal stresses to gain a direct understanding of interface motion and healing.

Continuous sliding of shear interfaces

We test the concepts of static friction, continuous diminishing sliding during holds and healing by considering seemingly stationary frictional interfaces in the laboratory. Two equal-sized poly(methyl methacrylate) (PMMA) plates are in contact over an interface with an inclination angle α, with the setup analogous to a block on the inclined plane (Fig. 1a,d). This experimental setup has been used to study key issues of frictional sliding and rupture dynamics, including the sub-Rayleigh to supershear rupture transition[41], pulse-like and crack-like rupture modes[46],

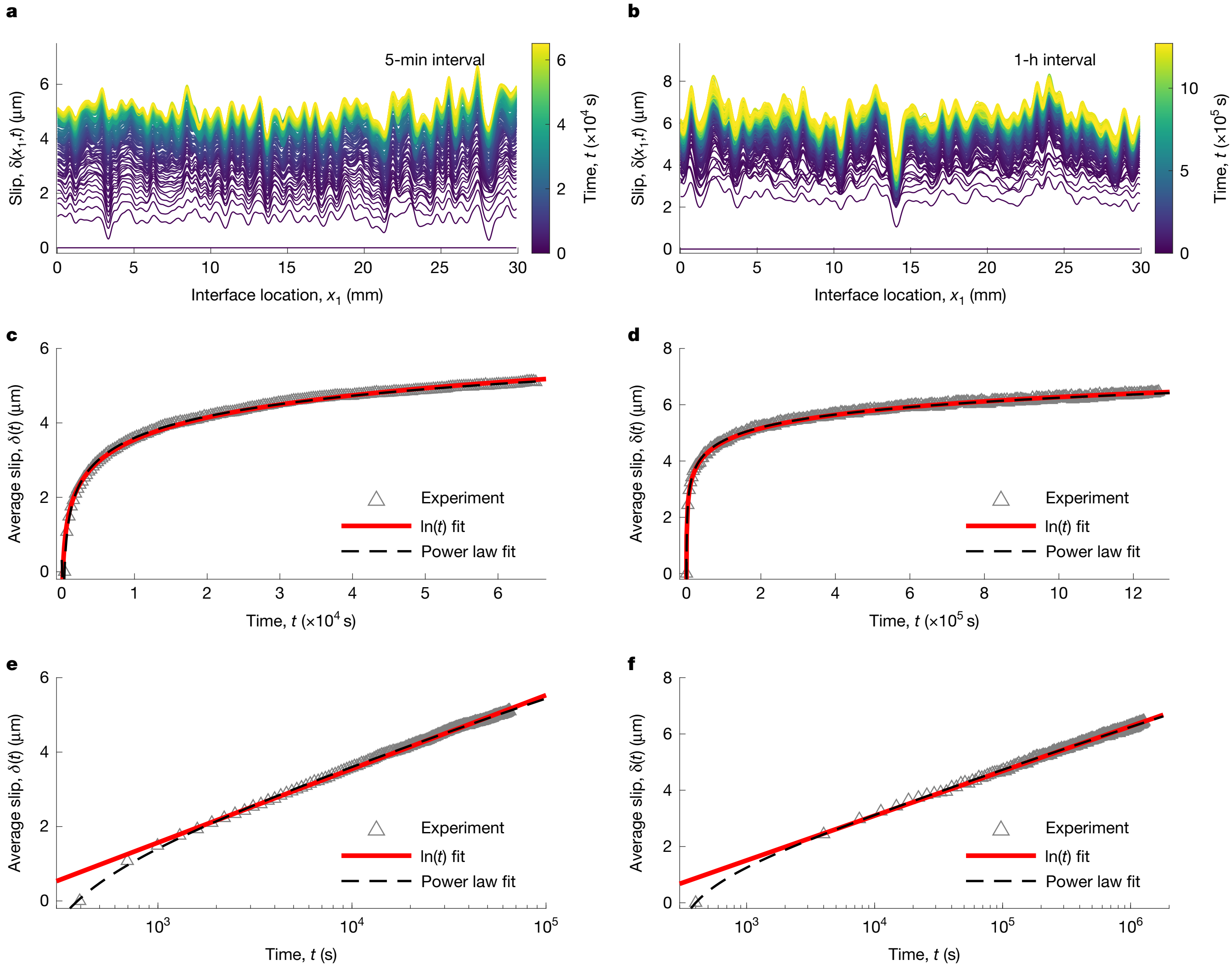

Fig. 2 | Experimental measurements showing continuous sliding of nominally stationary frictional interfaces. a,**b**, Accumulating slip $\delta(x_1, t)$ along the PMMA interfaces colour-coded by time, from two distinct experiments, one over 18 h (6.48×10^4 s) (left) and another over 2 weeks (1.21×10^6 s) (right). **c**,**d**, The corresponding evolution of the spatially averaged slip $\delta(t)$ (triangles). The average slip is fitted using predicted functions from RSF, with logarithmic functions arising from the velocity-neutral ($a = b$) assumption (red lines) and power-law functions arising from the ageing state evolution law when $V\theta/D_{RS} \ll 1$ ($\theta = t$ approximation) (dashed black lines). **e**,**f**, The same results with the time on the log scale, emphasizing that power laws provide a better fit.

evolution of dynamic friction[17], slip induced by fluid injection[47] and effects of rock gouge[48]. The specimen is compressed by a vertical load $P = 10$ MPa, resulting in resolved shear and normal stresses $\sigma_0 = P\cos^2\alpha$ and $\tau_0 = P\sin\alpha\cos\alpha$ with the ratio $\tau_0/\sigma_0 = \tan\alpha$. We study interfaces with values of α such that the ratio of the resolved shear to normal stresses is less than the classically defined static friction coefficient f_s, that is, $\tan\alpha < f_s = \tan\alpha_{crit}$. To determine α_{crit}, we conduct a series of experiments incrementally increasing the inclination angle α until the surface starts to visibly slip during loading. We find this critical angle (α_{crit}) to be 30° and therefore $f_s = \tan\alpha_{crit} = 0.58$. Hence, we select an angle $\alpha = 26°$ for our study, with $\tan 26° = 0.49$ being notably smaller than the static friction coefficient f_s. To put the difference in friction coefficient of about 0.1 in perspective, its product with an average compressive stress of 100–200 MPa over the seismogenic depths would result in shear stress changes of about 10–20 MPa, whereas the average shear stress change in earthquakes is 1–10 MPa (ref. 49).

Once the target load P is reached, the specimen is left untouched for 18 h in one type of experiment and 2 weeks in another, with the load kept constant using the automatic load control. Six repeated 18-h tests and one 2-week test are conducted. We measure the amount of interfacial sliding from the digital image correlation (DIC) analysis[32] of optical images taken at the centre of the specimen every 5 min over a field of view of 30×22 mm^2 (Fig. 1d and Extended Data Fig. 1). As a result, we can track the full-field distributions of displacements over the entire field of view (Fig. 1e, Extended Data Tables 1 and 2 and Methods). We have successfully used this approach to quantify the full-field behaviour of dynamic ruptures[18,31] and characterize the evolution of dynamic friction[17,48]. The relative sliding (slip) at the interface is obtained locally from the difference of the displacement component in the interface-parallel direction, measured immediately above and below the interface. The ability to perform these local measurements is a key advantage compared with most frictional experiments that infer slip from far-field measurements of the load-point displacement.

Our measurements show that the PMMA interfaces exhibit continuous sliding over the entire duration of the experiments (Fig. 2), in contradiction to the notion of static friction and laws that incorporate it, such as commonly used slip-weakening friction[37,38]. Tracing slip distributions over the interface at equally spaced time instants shows curves clustering with increasing time. This indicates that slip rates are decreasing with time, consistent with RSF formulations that predict these interfaces should be healing with time. Mathematically, this is expressed through the increasing state variable, which results in the decay of slip rates to add up to the same resolved shear stress in equation (1). Falling slip rates with time are also shown by the time histories of the average cumulated slip $\delta(t)$, with $\delta(t) = \frac{1}{L}\int \delta(x_1, t)\mathrm{d}x_1$ (Fig. 2c,d).

After 18 h of hold time, the average accumulated slip δ ranges from 4 µm to 6 µm for bare PMMA surfaces. Only a minute part (<0.05 µm) of the slip budget can be accommodated by viscoelastic relaxation of the specimens across the distance at which the slip is computed (1 pixel or 15 µm), as shown by tests conducted on specimens without interface and in which no frictional sliding is present (Methods and Extended Data Fig. 2a,b). Moreover, the sharp discontinuity in the displacement field across the interface (Methods and Extended Data Fig. 2c,d) indicates that shear-induced deformation of the material near the interface contributes a negligible portion of the slip budget and that sliding occurs across a region that is less than 1 pixel (15 µm) thick. The averaged slip evolution for different tests under the same conditions is also similar (Extended Data Fig. 3).

Continuous sliding of granular materials

To provide an analogue of natural earthquake faults, we have also conducted 18-h experiments with a rock gouge layer filling most of the interface (Fig. 3a and Methods). Gouge is the fine granular material present in faults in the crust of Earth, produced by comminution during sliding[4,50]. The fault gouge layer exhibits the same qualitative behaviour as the bare PMMA interface, with continuously accumulating slip that slows down with time (Fig. 3b,c). Given the time dependence of the measured relative displacement, it cannot be because of elastic deformation of the gouge layer, which would occur at the beginning of the hold. The difference between the gouge experiments and the PMMA-interface experiments is that the former visibly slips during loading as well, and then results in a much larger net slip for the same amount of monitored time. Yet they appear nominally stationary at the end of the experiment, at 18 h, when their slip rate reduces to nearly 10^{-10} m s^{-1}. Therefore, their behaviour also violates the notion of static friction coefficient as the interfaces first appear to slide and then not at the same ratio of shear to normal stress.

Explaining slip rate with a friction law

Although both the observed accumulating slip and decrease in slip rate are qualitatively consistent with RSF formulations, let us demonstrate this more quantitatively using our experiments on the PMMA interfaces. To match the measured slip rate evolution with the RSF formulation, we can change four rate-and-state parameters and one initial condition (for the history-dependent state variable). To identify all possible parameter values consistent with our observations, we can conduct a comprehensive grid search over this parameter space by numerically iterating between equations (1) and (2) (or equations (1) and (3)). However, here we consider two scenarios for which closed-form analytical solutions do exist, allowing us to invert the best-fit parameters for these scenarios directly from the data.

The first scenario assumes that the frictional interface is velocity-neutral ($a = b$), that is, friction does not depend on slip rate in the steady state. In such a case, the cumulated slip is predicted to increase logarithmically with time as

$$\delta(t) = C_1 \ln(t + t_0) + C_2 \tag{4}$$

where constant C_1 is a function of rate-and-state parameter a, critical slip distance D_{RS} and reference friction coefficient f^* that depends on the state evolution law. C_2 is an integration constant that depends on initial

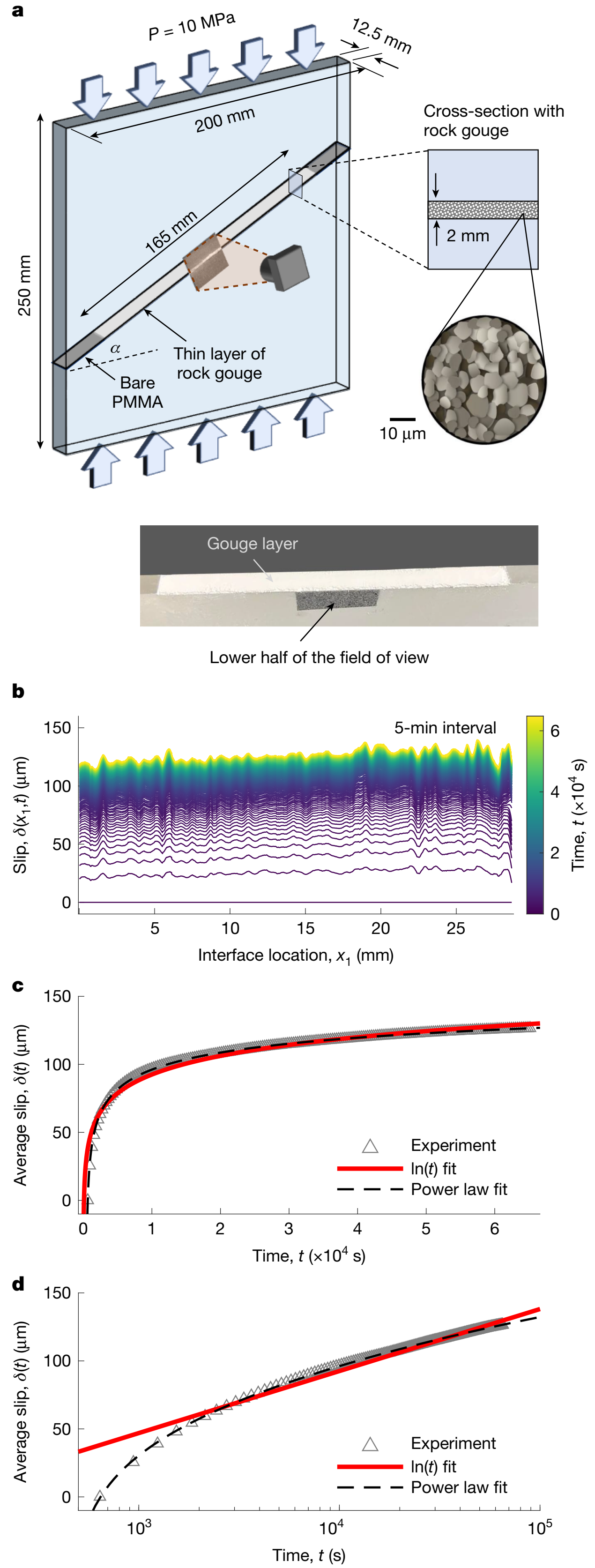

Fig. 3 | Interfaces with rock gouge sliding with decaying rates under the same loading conditions. **a**, Experimental setup featuring rock gouge layer embedded within the PMMA interface. **b**, Accumulating slip $\delta(x_1, t)$ along the interface colour-coded with time. **c**, The corresponding evolution of the average slip across the gouge layer (triangles). The fits are as in Fig. 2c–d. **d**, The same results with the time on a log scale, emphasizing that power laws provide a better fit.

conditions. The initial condition t_0 is equal to $\theta_{\min} D_{\mathrm{RS}} \exp((f - f^*)/a)/C_1$, where $\theta_{\min}$ is the value of the state variable just after the two surfaces come in contact during loading (Methods). We find $t_0 \approx 10^{-14}$ s, and therefore, negligible values of $\theta_{\min}$. The logarithmic fit captures the qualitative features of the accumulating slip but substantially diverges from the measurements during early times (Fig. 2e,f, Extended Data Fig. 3 and Supplementary Fig. 1), underpredicting the slip in the middle part of the experiment and overpredicting it towards the end. The misfit suggests that, under our experimental conditions, the interface is not exactly velocity-neutral.

The second scenario assumes that the value of the state variable θ is equal to time t, as would be approximately correct for the ageing form of the state variable evolution for small enough slip rates. If $V\theta/D_{\mathrm{RS}} \ll 1$, the ageing form reduces to $\mathrm{d}\theta/\mathrm{d}t = 1$ and the state variable grows with time. With this approximation, slip evolves as a power law of time:

$$\delta(t) = C_1(t - t_0)^{C_3} + C_2 \tag{5}$$

where C_1 is a function of a, D_{RS} and f^*, $C_3 = 1 - b/a$, and C_2 and t_0 depend on the initial conditions representing the approximate time after which the $V\theta/D_{\mathrm{RS}} \ll 1$ approximation becomes accurate (Methods). In particular, parameter C_3 can be used to constrain the ratio b/a and determine whether the interface is velocity-weakening ($a < b$), velocity-neutral ($a = b$) or velocity-strengthening ($a > b$). We find a near-perfect fit (Fig. 2e,f, Extended Data Fig. 4 and Supplementary Fig. 2). A better fit than the first scenario is expected because this scenario contains more fitting parameters. The fit is nonunique, in that similar errors can be achieved for different combinations of the rate-and-state parameters (Extended Data Fig. 5). The best-fit value of t_0 is about 5 min. Evaluation of the $V\theta/D_{\mathrm{RS}}$ term shows that it decays to values smaller than 0.1 after 4.5 min, for a typical value of $D_{\mathrm{RS}} \approx 10$ μm (Methods and Extended Data Fig. 6). Furthermore, the best fit suggests that PMMA interface is close to velocity-neutral and only slightly velocity-weakening, consistent with the first approximate approach. We note that this fit assumes that interface healing—and the state variable evolution—occurs mainly with time. Recent experimental studies indicate that healing in rock may occur predominantly with slip[16], and there is no guarantee that the mechanisms of state evolution are the same across materials. Although the fit here is done mainly to illustrate that the results are consistent with the rate-and-state framework, it would be important to develop more general fitting procedures.

The slip evolution of interfaces embedded with rock gouge also shows quantitative adherence to the rate-and-state framework, as they can be well-explained with a logarithmic function (equation (3), Fig. 3c,d and Extended Data Fig. 7), and even more so with the power law (equation (4), Fig. 3c,d and Extended Data Fig. 8). However, the experiments with gouge exhibit significantly more slip than those with purely PMMA interfaces (compare Fig. 3c with Fig. 2c), implying different frictional properties. Experiments with gouge, which contain both bare PMMA and gouge interface portions, probably result in slip variations along the interface of the experimental sample, potentially resulting in redistribution of shear stress along the interface and evolution of shear stress with time at the measurement locations. Therefore, the corresponding frictional parameters cannot be deduced using the method presented here, which assumes that the shear stress is uniform along the interface and equal to the resolved shear stress because of far-field loading. This can be remedied in future experiments by incorporating rock gouge over the entire interface.

As the power-law fit explains our observations well, we compute the temporal evolution of slip rates using time derivatives of the best power-law fit of slip (Fig. 4a,b). We find that, after 18 h of hold time, the interfaces are still sliding, with the slip rates decaying by more than three orders of magnitude, starting from 10^{-7} m s^{-1} and reaching values of 10^{-11} m s^{-1} and 10^{-10} m s^{-1} for bare PMMA and for rock gouge interfaces, respectively (Fig. 4a). Furthermore, the (separate) 2-week-long test with bare PMMA interfaces picks up right where the 18-h test ends, with slip rate decreasing another order of magnitude but never reaching zero (Fig. 4b). The fact that we find very similar slip rate decay curves for the series of repeated tests confirms the repeatability of the experimental findings. The measurement of miniscule slip rates (10^{-12} m s^{-1}) and repeatability are enabled by a meticulous experimental procedure involving highly tailored DIC analysis and a strict protocol for the preparation of the frictional interfaces.

Diminishing slip rate captures healing

Our setup features a unique scenario in which the friction coefficient (ratio of shear to normal stress) remains constant throughout the experiments, even during the initial loading phase. This provides a unique opportunity for us to directly quantify healing, as the decaying slip rates $V(t)$ directly reflect the increasing state variable $\theta(t)$. With respect to a reference value of slip rate V_0 at state variable θ_0, the evolution of the state variable can be rewritten from equation (1) as follows:

$$\left(\frac{\theta(t)}{\theta_0}\right)^{\frac{b}{a}} = \frac{V_0}{V(t)} \tag{6}$$

This means that we can visualize the interface healing by interpreting the measured slip rates in terms of the evolution of the state variable that records healing (Fig. 4c). Therefore, the experiments developed here provide opportunities for direct quantification of state variable evolution and healing without the need for inferring it from modelling.

A consequence of healing is the higher peak friction for a more healed interface[15,27,33]. Assuming reasonable rate-and-state parameters for PMMA consistent with our fits ($a = 0.008$, $a - b = -0.001$, $D_{\mathrm{RS}} = 2$ μm, $V^* = 1$ μm s^{-1}, $f^* = 0.50$) and ageing law[26], we determine the evolution of friction compared with slip if the slip rate were to jump to 1 m s^{-1}, an average slip rate during earthquake ruptures[49]. For an increase in the hold times from 20 min to 1 year, the peak friction is expected to increase by 0.09 (Fig. 4d). This increase in friction with hold times is consistent with the results of the slide–hold–slide experiments[15,33]. This translates to peak shear resistance increases of about 10–20 MPa at seismogenic depths, much larger than the average stress drops of 3 MPa for earthquakes[49], highlighting the importance of healing in geologic faults. Furthermore, if we approximate the friction evolution with linear slip-weakening laws[37,38], the slip-weakening distance D_c (amount of slip required for τ_{peak} to weaken to τ_{d}, which is distinguishable from D_{RS} in the rate-and-state formulation) would also increase by 20 μm, from 40 μm to 60 μm, and the breakdown energy associated with the cohesive zone, $G = \frac{1}{2}(\tau_{\mathrm{peak}} - \tau_{\mathrm{d}})D_c$, would increase by 4.5 J m^{-2}, from 3.5 J m^{-2} to 8 J m^{-2}. Although slip-weakening laws can be a good approximation for modelling friction, their parameters should not be constant in time but rather depend on the state of the interfaces and the sliding processes. Note that the increase in peak friction would be the same for the slip law but the change in D_c would be much smaller[3] (Supplementary Fig. 3).

Implications for earthquake processes

Although previous studies indicate that the concepts of static friction do not capture the entire frictional behaviour[13,21,26,27], this concept is still widely used to model earthquakes and landslides[35,36]. Our experiments provide direct measurements that nominally stationary frictional interfaces—with driving forces below static friction—are sliding with diminishing slip rates, and hence also healing. By using local interfacial sliding measurements of unprecedented accuracy, we demonstrate that, under shear, nominally stationary bare frictional interfaces and those embedded with granular materials are sliding with decreasing slip rates, imperceivable to the eye, that can only be measured with an

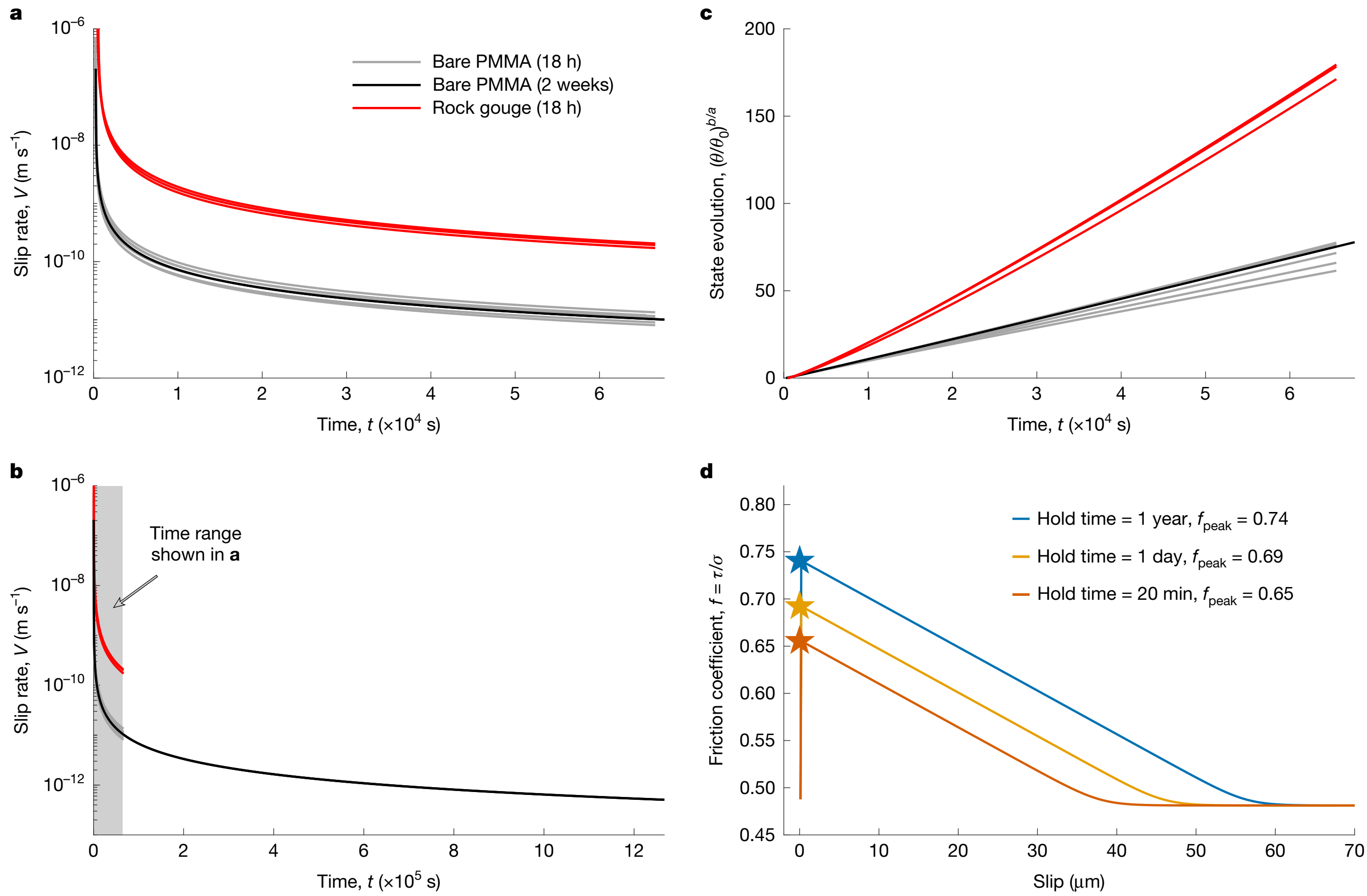

Fig. 4 | Nonzero, diminishing slip velocity of nominally stationary interfaces validates the rate-and-state formulation and captures healing. a,**b**, The evolution of slip rate for all experiments (six 18-h and one 2-week experiments for PMMA interfaces and three 18-h experiments for rock gouge) obtained by differentiating the best power-law fit of slip. The experiments are highly repeatable and are consistent with the rate-and-state framework. **c**, Healing is recorded by increases in the state variable, which can be inferred directly from our measurements without assuming any form for the state evolution law. θ_0 is chosen to be the state variable at $t_0 = 20$ min. **d**, Rapid velocity jump to a slip rate of 1 m s^{-1}, average for earthquake rupture, after longer hold times would result in significantly higher peak friction and larger effective fracture energy.

extremely accurate technique. This is true even when the ratio of shear to normal stress is lower than the classically defined static friction coefficient, measured for PMMA based on the critical-angle concept. Our experimental observations can be fitted with RSF formulations but cannot be explained by laws that incorporate the concept of static friction such as the widely used slip-weakening laws. The decrease of slip rates with time allows us to infer the increase in the state variable and hence quantify interface healing. Our findings suggest that the prediction of RSF that interfaces under shear are always sliding is not an artefact—as still commonly assumed —and holds down at least to slip rates of the order of 10^{-12} m s^{-1}. Although these slip rates may be negligible for some applications, they are crucial for understanding earthquake nucleation[2,3,20] as well as for validation of the RSF formulation, which posits that the properties of frictional interfaces change even when they appear stationary, in terms of decreasing slip rates and increasing values of the state variable that record healing. The healing then manifests itself in terms of higher peak friction during more rapid sliding episodes[15,27,33], and initial strength excess that needs to be exceeded before induced earthquakes in tectonically inactive areas can start nucleating[24,25], making earthquake hazard dependent on the amount of healing. Furthermore, our experiments on nominally stationary interfaces give access to very small slip rates V down to 10^{-12} m s^{-1} that have never been reported in a frictional study. Therefore, our experimental procedure can serve as a complementary method to constrain frictional parameters and study different state evolution laws. By combining our experiments with classical velocity-jump experiments[26,27] ($V \approx 10^{-6}$ m s^{-1}) and dynamic rupture experiments[17,48] ($V \approx 1$ m s^{-1}), we can enhance our understanding of how friction behaves across different scales of slip rates with far-ranging implications from engineering to geoscience.

Online content

Any methods, additional references, Nature Portfolio reporting summaries, source data, extended data, supplementary information, acknowledgements, peer review information; details of author contributions and competing interests; and statements of data and code availability are available at https://doi.org/10.1038/s41586-025-08673-0.

1. Rice, J. R. & Ruina, A. L. Stability of steady frictional slipping. *J. Appl. Mech.* **50**, 343–349 (1983).
2. Dieterich, J. H. in *Treatise on Geophysics* 2nd edn (ed. Schubert, G.) Vol. 4, 93–110 (Elsevier, 2007).
3. Ampuero, J.-P. & Rubin, A. M. Earthquake nucleation on rate and state faults – aging and slip laws. *J. Geophys. Res. Solid Earth* **113**, 2007JB005082 (2008).
4. Scholz, C. H. *The Mechanics of Earthquakes and Faulting* (Cambridge Univ. Press, 2019).
5. Handwerger, A. L., Rempel, A. W., Skarbek, R. M., Roering, J. J. & Hilley, G. E. Rate-weakening friction characterizes both slow sliding and catastrophic failure of landslides. *Proc. Natl Acad. Sci. USA* **113**, 10281–10286 (2016).
6. Zoet, L. K. & Iverson, N. R. A healing mechanism for stick-slip of glaciers. *Geology* **46**, 807–810 (2018).
7. Thøgersen, K., Gilbert, A., Schuler, T. V. & Malthe-Sørenssen, A. Rate-and-state friction explains glacier surge propagation. *Nat. Commun.* **10**, 2823 (2019).

8. Kinkaid, N. M., O'Reilly, O. M. & Papadopoulos, P. Automotive disc brake squeal. *J. Sound Vib.* **267**, 105–166 (2003).
9. Rabinowicz, E. Stick and slip. *Sci. Am.* **194**, 109–119 (1956).
10. Dowson, D. *History of Tribology* 2nd edn (Wiley, 1998).
11. Bhattacharya, P. & Viesca, R. C. Fluid-induced aseismic fault slip outpaces pore-fluid migration. *Science* **364**, 464–468 (2019).
12. Lapusta, N., Rice, J. R., Ben-Zion, Y. & Zheng, G. Elastodynamic analysis for slow tectonic loading with spontaneous rupture episodes on faults with rate- and state-dependent friction. *J. Geophys. Res.* **105**, 23765–23789 (2000).
13. Rice, J. R., Lapusta, N. & Ranjith, K. Rate and state dependent friction and the stability of sliding between elastically deformable solids. *J. Mech. Phys. Solids* **49**, 1865–1898 (2001).
14. Dieterich, J. H. A constitutive law for rate of earthquake production and its application to earthquake clustering. *J. Geophys. Res.* **99**, 2601–2618 (1994).
15. Marone, C. The effect of loading rate on static friction and the rate of fault healing during the earthquake cycle. *Nature* **391**, 69–72 (1998).
16. Bhattacharya, P., Rubin, A. M., Tullis, T. E., Beeler, N. M. & Okazaki, K. The evolution of rock friction is more sensitive to slip than elapsed time, even at near-zero slip rates. *Proc. Natl Acad. Sci. USA* **119**, e2119462119 (2022).
17. Rubino, V., Rosakis, A. J. & Lapusta, N. Understanding dynamic friction through spontaneously evolving laboratory earthquakes. *Nat. Commun.* **8**, 15991 (2017).
18. Rosakis, A. J., Rubino, V. & Lapusta, N. Recent milestones in unraveling the full-field structure of dynamic shear cracks and fault ruptures in real-time: from photoelasticity to ultrahigh-speed digital image correlation. *J. Appl. Mech.* **87**, 030801 (2020).
19. Leeman, J. R., Saffer, D. M., Scuderi, M. M. & Marone, C. Laboratory observations of slow earthquakes and the spectrum of tectonic fault slip modes. *Nat. Commun.* **7**, 11104 (2016).
20. Gvirtzman, S. & Fineberg, J. Nucleation fronts ignite the interface rupture that initiates frictional motion. *Nat. Phys.* **17**, 1037–1042 (2021).
21. Ruina, A. Slip instability and state variable friction laws. *J. Geophys. Res.* **88**, 10359–10370 (1983).
22. Ader, T. J., Lapusta, N., Avouac, J.-P. & Ampuero, J.-P. Response of rate-and-state seismogenic faults to harmonic shear-stress perturbations. *Geophys. J. Int.* **198**, 385–413 (2014).
23. Sirorattanakul, K. et al. The 2020 Westmorland, California earthquake swarm as aftershocks of a slow slip event sustained by fluid flow. *J. Geophys. Res. Solid Earth* **127**, e2022JB024693 (2022).
24. Acosta, M. et al. Earthquake nucleation characteristics revealed by seismicity response to seasonal stress variations induced by gas production at Groningen. *Geophys. Res. Lett.* **50**, e2023GL105455 (2023).
25. Heimisson, E. R., Smith, J. D., Avouac, J.-P. & Bourne, S. J. Coulomb threshold rate-and-state model for fault reactivation: application to induced seismicity at Groningen. *Geophys. J. Int.* **228**, 2061–2072 (2022).
26. Dieterich, J. H. Modeling of rock friction: 1. Experimental results and constitutive equations. *J. Geophys. Res.* **84**, 2161 (1979).
27. Marone, C. Laboratory-derived friction laws and their application to seismic faulting. *Annu. Rev. Earth Planet. Sci.* **26**, 643–696 (1998).
28. Rabinowicz, E. The nature of the static and kinetic coefficients of friction. *J. Appl. Phys* **22**, 1373–1379 (1951).
29. Gu, J.-C., Rice, J. R., Ruina, A. L. & Tse, S. T. Slip motion and stability of a single degree of freedom elastic system with rate and state dependent friction. *J. Mech. Phys. Solids* **32**, 167–196 (1984).
30. Daub, E. G. & Carlson, J. M. A constitutive model for fault gouge deformation in dynamic rupture simulations. *J. Geophys. Res. Solid Earth* **113**, 2007JB005377 (2008).
31. Rubino, V., Rosakis, A. J. & Lapusta, N. Full-field ultrahigh-speed quantification of dynamic shear ruptures using digital image correlation. *Exp. Mech.* **59**, 551–582 (2019).
32. Sutton, M. A., Orteu, J.-J. & Schreier, H. W. *Image Correlation for Shape, Motion and Deformation Measurements* (Springer, 2009).
33. Beeler, N. M., Tullis, T. E. & Weeks, J. D. The roles of time and displacement in the evolution effect in rock friction. *Geophys. Res. Lett.* **21**, 1987–1990 (1994).
34. Barbot, S., Lapusta, N. & Avouac, J.-P. Under the hood of the earthquake machine: toward predictive modeling of the seismic cycle. *Science* **336**, 707–710 (2012).
35. Lacroix, P., Handwerger, A. L. & Bièvre, G. Life and death of slow-moving landslides. *Nat. Rev. Earth Environ.* **1**, 404–419 (2020).
36. Dempsey, D. & Suckale, J. Physics-based forecasting of induced seismicity at Groningen gas field, the Netherlands. *Geophys. Res. Lett.* **44**, 7773–7782 (2017).
37. Ida, Y. Cohesive force across the tip of a longitudinal-shear crack and Griffith's specific surface energy. *J. Geophys. Res.* **77**, 3796–3805 (1972).
38. Palmer, A. C. & Rice, J. R. The growth of slip surfaces in the progressive failure of over-consolidated clay. *Proc. R. Soc. Lond. A* **332**, 527–548 (1973).
39. Freund, L. B. *Dynamic Fracture Mechanics* (Cambridge Univ. Press, 1990).
40. Ohnaka, M. A constitutive scaling law and a unified comprehension for frictional slip failure, shear fracture of intact rock, and earthquake rupture. *J. Geophys. Res.* **108**, 2000JB000123 (2003).
41. Xia, K., Rosakis, A. J. & Kanamori, H. Laboratory Earthquakes: the sub-Rayleigh-to-supershear rupture transition. *Science* **303**, 1859–1861 (2004).
42. Nakatani, M. Conceptual and physical clarification of rate and state friction: frictional sliding as a thermally activated rheology. *J. Geophys. Res* **106**, 13347–13380 (2001).
43. Marone, C. J., Scholtz, C. H. & Bilham, R. On the mechanics of earthquake afterslip. *J. Geophys. Res. Solid Earth* **96**, 8441–8452 (1991).
44. Bürgmann, R. et al. Earthquake potential along the Northern Hayward Fault, California. *Science* **289**, 1178–1182 (2000).
45. Perfettini, H. et al. Seismic and aseismic slip on the Central Peru megathrust. *Nature* **465**, 78–81 (2010).
46. Lu, X., Lapusta, N. & Rosakis, A. J. Pulse-like and crack-like ruptures in experiments mimicking crustal earthquakes. *Proc. Natl Acad. Sci. USA* **104**, 18931–18936 (2007).
47. Gori, M., Rubino, V., Rosakis, A. J. & Lapusta, N. Dynamic rupture initiation and propagation in a fluid-injection laboratory setup with diagnostics across multiple temporal scales. *Proc. Natl Acad. Sci. USA* **118**, e2023433118 (2021).
48. Rubino, V., Lapusta, N. & Rosakis, A. J. Intermittent lab earthquakes in dynamically weakening fault gouge. *Nature* **606**, 922–929 (2022).
49. Shearer, P. M. *Introduction to Seismology* (Cambridge Univ. Press, 2019).
50. Chester, F. M. & Chester, J. S. Ultracataclasite structure and friction processes of the Punchbowl fault, San Andreas system, California. *Tectonophysics* **295**, 199–221 (1998).

Methods

Specimen preparation

In this study, we investigate two different types of frictional interfaces under shear: (1) bare surfaces of PMMA and (2) rock gouge layer embedded in a PMMA sample. The specimens are cut from a PMMA sheet of size 250 mm × 200 mm × 12.5 mm to two equal-sized quadrilateral plates at an oblique inclination angle $\alpha = 26°$ using a computer numerical control machine. The inclined mating faces represent the frictional interfaces.

To ensure experimental reproducibility, the mating surfaces of the PMMA specimens are prepared following a well-developed surface finish procedure[31,51,52]. The interfaces are first polished to near-optical grade finish using a 100 rpm rotating polishing wheel covered with Buehler 12-inch Microcloth and soaked with a mixture of water and cerium oxide polishing compound (Buehler MiroMet) in the ratio of 2:1, achieving a typical roughness $R = \frac{1}{L}\int_0^L |z(x)|\mathrm{d}x \sim 0.016$ µm. Then, the interfaces are roughened by blasting with McMaster Carr abrasive glass beads with 70–140 mesh size corresponding with the diameter ranging between 104 µm and 211 µm using a pressure of 75 psi for 3 min. A similar procedure performed on a similar material (Homalite-100) generally achieves a typical roughness of $R \sim 0.5$ µm (ref. 51).

The rock gouge layer is incorporated into the PMMA sample using a hybrid configuration[48] and it covers 74% of the centre portion of the interface (165 × 12.5 mm^2 out of 222.5 × 12.5 mm^2) (Fig. 1d). The bare PMMA portion helps to maintain the inclination angle $\alpha = 26°$. The layer of rock gouge has a thickness of 2 mm, and it is composed of a fine quartz gouge power (MIN-U-SIL 10, commercially available from US Silica) with >99.5% silicon dioxide (SiO_2) and >96% of grains with a diameter of <10 µm. The field of view captured by the camera (30 × 22 mm^2) falls entirely within the gouge portion at the centre of the interface, away from the transitional boundaries between gouge and bare PMMA. Rock gouge is incorporated along the PMMA interface following a similar procedure to that outlined in ref. 48. First, 1 mm of PMMA is removed along the portion to be filled with gouge, for each mating half. A fine mist of glue is sprayed along this portion, and the specimen is pressed against gouge particles laid on a flat surface at room temperature and humidity. Isopropyl alcohol is used to clean gouge particles on the unmilled portion of bare PMMA. A razor blade is used to shave off excess particles over the milled portion to ensure that the gouge surface is flush with bare PMMA. The glue adheres a thin layer of gouge particles to the PMMA, preventing shear failure from occurring at the gouge–PMMA interface and allowing us to study the frictional behaviour of rock gouge.

Loading and image acquisition protocols

To apply shear stress on the frictional interfaces, the two mating halves are first placed into contact and aligned using a specimen holder to ensure parallel loading surfaces and to prevent specimen buckling. The assembly is loaded uniaxially and uniformly using an Instron 300LX with a constant loading rate of 0.2 mm min^{-1} (corresponding to vertical strain rates of 1.3×10^{-5} s^{-1}, well within the quasi-static regime) until the vertical-load $P = 10$ MPa is reached. The loading process takes approximately 6 min and 10 min for specimens with bare PMMA and with interbedded rock gouge surfaces, respectively. The loading time is longer for specimens with rock gouge because more vertical displacement is required to compact the rock gouge layer, because of its granular nature. Both surfaces are inclined at an angle $\alpha = 26°$, at which the vertical load P produces a resolved shear stress of $\tau_0 = P \sin\alpha \cos\alpha = 3.94$ MPa and a normal stress of $\sigma_0 = P\cos^2\alpha = 8.08$ MPa. The load is then maintained constant for 18 h in most experiments and for 2 weeks in one experiment using an automatic load control system.

The central portion of the specimen is monitored using optical imaging with a field of view of 30 × 22 mm^2, starting when the vertical load P is reached. To provide the characteristic texture required for performing image correlation, the field of view is covered with small black random speckles over a thin white coating produced with Krylon sprays. The average speckle size produced by the Krylon spray spans 5 pixels, with 1 pixel corresponding to approximately 15 µm. Every 5 min, 32 images of size 2,048 × 1,536 pixels^2 are taken at a rate of approximately 50 fps using the Imaging Source monochrome camera DMK 37BUX250. The camera is equipped with a Schneider Optics 50 mm Xenoplan compact series lens (21-1001976) and a 10 mm Tamron extension ring (Extended Data Table 1). Typically, once the target load is attained, 217 sets of 32 images are acquired every 5 min during each test over the 18 h span duration (Extended Data Fig. 1). To reduce the noise level, each set of 32 images is numerically averaged using the Imaging Source software IC Capture v.2.4 and only the averaged images are used for the analysis. To obtain full-field displacements and slip along the interface, the sequence of 217 averaged digital images is analysed using DIC, as detailed in the next section. Six independent but nominally identical 18-h experiments are performed for the bare PMMA interface and three for the interface embedded with rock gouge to check the repeatability. Moreover, one 2-week experiment is conducted for the bare PMMA interface.

From optical images to cumulated interfacial slip

To measure slip along the frictional interface, the optical images are analysed using the DIC technique[32]. Using Correlated Solutions VIC-2D commercial image-matching software, we produce an evolving sequence of full-field displacements for each experiment. The first image in the sequence is used as a reference image in the correlation for bare PMMA, whereas the last image is used as a reference image in the case of rock gouge to prevent decorrelations because of large displacements in the later images. To preserve the discontinuity of displacements across the interface, the correlation analysis is performed over two domains separated by the interface[17,31,48,53,54]. For surfaces with rock gouge, the 2-mm gouge layer is treated as an infinitesimal layer and excluded from the correlation. Moreover, to make the correlations computationally amenable, only subregions of size 2,048 × 150 pixel^2 on the different sides of the interface are considered. The correlation uses a subset size of 41 × 41 pixels^2 and a step of 1 pixel. The Fill Boundary algorithm is used to extrapolate correlated displacements from half a subset size away from the interface to directly at the interface (Extended Data Table 2). Using this approach, we can resolve minute full-field displacements as small as 1×10^{-3} of the pixel size in the optimal scenario[31], equivalent to 0.015 µm for our field of view. For the 2-week experiment, to reduce computation time, only images taken every hour are kept and analysed.

Using full-field displacements, accumulated interfacial slip δ is calculated by taking the differences between the interface-parallel displacements u_1 of pixels immediately below and above the interface, that is, $\delta(x, t) = u_1(x_1, x_2 = 0^-, t) - u_1(x_1, x_2 = 0^+, t)$. To describe the macroscopic frictional behaviour of the interface, the average accumulated slip $\delta(t)$ is calculated for each time frame, that is, $\delta(t) = \frac{1}{L}\int_0^L \delta(x_1, t)\mathrm{d}x_1$.

Uncertainty quantification of slip measurements

To quantify measurement uncertainties, we perform an experiment on a PMMA sample without an interface, under the same loading conditions as the regular experiments and we measure slip along the mathematical line where an interface lies in the regular experiment following the same analysis procedure. Since there is no physical interface in this case, any measured slip is due to the DIC measurement accuracy or to the viscoelastic relaxation of PMMA over the distance across which slip is computed, which is 1 pixel (15 µm). The DIC measurement accuracy is affected by a number of factors, such as the electronic noise of the camera sensor, lighting variations during the observation time window, vibrations of the optical table, suboptimal speckle pattern or interpolation methods used during correlations[31,32,55]. In our case, we find that DIC measurement errors and viscoelastic relaxation contribute to less than 0.05 µm of the average accumulated slip (Extended Data Fig. 2).

Fitting the slip measurements

According to RSF formulations[1,13,21,26,27,56,57], which have been developed based on previous laboratory experiments sliding two rock surfaces or a gouge layer, friction coefficient $f(t)$ depends on slip rate $V(t)$ and has memory effects captured by an evolving state variable $\theta(t)$. Equation (1) from the main text is an example. The velocity-dependent term (direct effect) is universally positive ($a > 0$) and can be interpreted as an instantaneous increase of local contact strength with an instantaneous increase in strain rate, which is a traditional material response that can often be described by a thermally activated Arrhenius process[13,42]. The state-dependent term (evolutionary effect) describes the evolution of contact population and properties that would occur after a change in slip rate, such as due to gradual dilation and/or compaction[58–60], until the steady-state conditions are reached that correspond to a new slip rate. In stationary or near-stationary contact, such as in our experiments, the state-dependent term reflects interface healing, interpreted as the growth of the real area of contact, for example, owing to thermally activated creep[61–65] or as increase in contact quality and hence strength, for example, owing to diffusion processes related to the formation of interfacial chemical bonds[66]. Two typical choices for the state evolution law include the ageing law[26] and the slip law[21], which are equations (2) and (3) in the main text.

At a steady state, that is, $\mathrm{d}\theta/\mathrm{d}t = 0$, both state evolution laws converge and $\theta = D_{RS}/V$ reflects the contact age. Moreover, the friction coefficient becomes purely rate-dependent:

$$f = f^* + (a-b)\ln\left(\frac{V}{V^*}\right) \tag{7}$$

If $a < b$, the friction coefficient at steady state decreases with slip rate and the interface is said to be velocity-weakening. By contrast, if $a > b$, friction increases with slip rate and the interface is velocity-strengthening. If $a = b$, friction does not change with slip rate and the interface is velocity-neutral. Stability analysis shows that unstable slip can occur only for a velocity-weakening interface[1,4].

A drawback of the logarithmic form (equation (1)) is that the friction f is not defined for $V = 0$, that is, the logarithmic function is undefined at zero. The logarithmic form was derived from purely empirical considerations to match experimental observations[21,26,67]. This form is consistent with an Arrhenius rate process at contact junctions in the range for which forward microscopic jumps, in the direction of shear stress, are overwhelmingly more frequent than backward jumps, and hence the backward jumps are ignored. This interpretation has been implicit or explicit in several studies[42,62,68–74]. Accounting for backward jumps, which are expected to be comparable with forward jumps near zero shear stress and zero slip rate, gives[12]

$$f(t) = a\,\mathrm{arcsinh}\left[\frac{V(t)}{2V^*}\exp\left(\frac{f^* + b\ln\left(\frac{V^*\theta(t)}{D_{RS}}\right)}{a}\right)\right] \tag{8}$$

This physically based regularized form highlights that exactly zero slip rates are only expected at zero shear stress, with any nonzero shear stress giving rise to some slip rate. Note that this regularized form is indistinguishable from the logarithmic form in the range of experimental observations. Therefore, we will continue to use the logarithmic form in our analysis.

Our slip measurements show that both bare PMMA surface and those embedded with rock gouge continue to slide over the duration of the experiments, although the friction coefficient is smaller than its static value and is a constant with time. RSF predicts that all interfaces are always sliding[27] and could potentially explain our observations. Rewriting equation (1) from the main text to solve for $V(t)$ yields

$$V(t) = V^*\exp\left(\frac{f-f^*}{a}\right)\left(\frac{V^*\theta(t)}{D_{RS}}\right)^{-\frac{b}{a}} \tag{9}$$

In general, no closed-form solutions exist for systems of equations: equations (2) and (9) or equations (3) and (9). Although it is possible to fit the slip measurements by using a grid search and fully evolve the state variable through a finite difference scheme, the number of free parameters results in many possible solutions. In the following subsections, we present two particular cases for which there exists a closed-form expression for $\theta(t)$, $V(t)$ and $\delta(t)$.

Closed-form expression of slip when $a = b$

Motivated by the approximately velocity-neutral behaviour of PMMA, we can assert a special case in which $a = b$. In this case, equation (9) simplifies to

$$V(t) = \exp\left(\frac{f-f^*}{a}\right)\frac{D_{RS}}{\theta(t)} \tag{10}$$

By substituting equation (10) into the state evolution laws (equations (2) and (3)), the time derivative of the state variable becomes time-independent, as follows:

$$\frac{\mathrm{d}\theta}{\mathrm{d}t} = 1 - \exp\left(\frac{f-f^*}{a}\right) = C_{\mathrm{ageing}} \tag{11}$$

$$\frac{\mathrm{d}\theta}{\mathrm{d}t} = \left(\frac{f^*-f}{a}\right)\exp\left(\frac{f-f^*}{a}\right) = C_{\mathrm{slip}} \tag{12}$$

Assuming that when we place the two halves of the specimen in contact at $t = 0$, the instantaneous contact area achieved produces the state variable $\theta = \theta_{\min}$, integrating equations (11) and (12) leads to

$$\theta(t) = C_{\mathrm{ageing/slip}}\,t + \theta_{\min} \tag{13}$$

where $C_{\mathrm{ageing/slip}}$ is C_{ageing} or C_{slip}, as defined in equations (11) and (12). Substituting equation (13) into (10) yields an expression for slip rate as a function of time:

$$V(t) = \frac{\exp\left(\frac{f-f^*}{a}\right)D_{RS}}{C_{\mathrm{ageing/slip}}\,t + \theta_{\min}} \tag{14}$$

Equation (14) can then be integrated to get the evolution of slip, $\delta(t)$, which can be rewritten as follows:

$$\delta(t) = C_1\ln(t+t_0) + C_2 \tag{15}$$

where $C_1 = D_{RS}/(\exp(\frac{f^*-f}{a}) - 1)$ and $t_0 = \theta_{\min}/C_{\mathrm{ageing}}$ for the ageing law and $C_1 = aD_{RS}/(f^*-f)$ and $t_0 = \theta_{\min}/C_{\mathrm{slip}}$ for the slip law. As C_1 is a function of a, D_{RS} and f^*, the value of C_1 that best fits the observations can be used to constrain these frictional parameters. Parameters t_0 and C_2, an integration constant, are related to the initial conditions of the system. This logarithmic form is similar to the postseismic relaxation that occurs in the form of creep on faults (afterslip) following large earthquakes[75]. We find the best-fit parameters through a Matlab fit function and explore the surrounding parameter space through a grid search. For bare PMMA surfaces, the search range is between 0 μm and 1.5 μm for C_1, between −100 μm and 100 μm for C_2, and between 0 h and 1 h for t_0. For surfaces embedded with rock gouge, the search range is between 0 μm and 50 μm for C_1, between −1,000 μm and 1,000 μm for C_2, and between 0 h and 10 h for t_0. The grid search results are shown in Extended Data Figs. 3 and 7, Supplementary Fig. 1 and Supplementary Tables 1 and 2.

Closed-form expression of slip when $\theta = t$

A different simplification arises in the ageing law framework when the state variable is approximately equal to time. Motivated by the slow slip rate expected from the experiment, we can explore the limiting case in which $V\theta/D_{RS} \ll 1$. In this case, the ageing law reduces to $d\theta/dt = 1$ and the state variable integrates to $\theta(t) = t - t_0$, for some integration constant t_0 representing the time at which the $V\theta/D_{RS} \ll 1$ approximation starts to become accurate. The expressions for slip rate (equation (10)) and slip become, respectively,

$$V(t) = V^{*}\exp\left(\frac{f-f^{*}}{a}\right)\left(\frac{V^{*}(t-t_0)}{D_{RS}}\right)^{-\frac{b}{a}} \quad (16)$$

$$\delta(t) = \left(\frac{a}{a-b}\right)V^{*}\exp\left(\frac{f-f^{*}}{a}\right)\left(\frac{V^{*}}{D_{RS}}\right)^{-\frac{b}{a}}(t-t_0)^{1-b/a} + C \quad (17)$$

The slip observations can then be fitted with a power-law relationship of the form

$$\delta(t) = C_1(t-t_0)^{C_3} + C_2 \quad (18)$$

from which b/a can be inferred from $C_3 = 1 - (b/a)$ and the frictional parameters a, D_{RS} and f^{*} can be constrained from $C_1 = (\frac{a}{a-b})\,V^{*}\exp(\frac{f-f^{*}}{a})\,(\frac{V^{*}}{D_{RS}})^{-\frac{b}{a}}$. As before, we find the best-fit parameters through a Matlab fit function and explore the surrounding parameter space through a grid search. For bare PMMA surfaces, the search range is between −50 and 50 μm $s^{-(1-b/a)}$ for C_1, between −200 μm and 200 μm for C_2, between −0.5 and 0.5 for C_3, and between −10 h and the time t at which we have the first image for t_0. For surfaces embedded with rock gouge, the search range is between −500 μm $s^{-(1-b/a)}$ and 500 μm $s^{-(1-b/a)}$ for C_1, between −2,000 μm and 2,000 μm for C_2, between −0.5 and 0.5 for C_3, and between −10 h and the time t at which we have the first image for t_0, which is typically 7 min for PMMA and 10 min for gouge. The upper bound constraint on t_0 prevents the argument of the power law (and hence the state variable $\theta(t)$) from becoming negative and is valid as long as the fitting does not return the upper bound as the best fit. The grid search results are shown in Extended Data Figs. 4 and 8, Supplementary Fig. 2 and Supplementary Tables 3–4.

There are ranges of parameters that would be unphysical according to the rate-and-state formulation. As we expect a, V^{*}, f^{*} and D_{RS} to be positive, we cannot have a velocity-strengthening interface ($a > b$) and $C_1 < 0$ or a velocity-weakening interface ($a < b$) and $C_1 > 0$ (Supplementary Fig. 2). This also ensures that slip accumulates monotonically over time. We also find that for any set of $C_1 > 0$ and $C_3 > 0$, there exists another pair of $C_1 > 0$ and $C_3 > 0$ that can fit the data almost as well (Extended Data Fig. 5), demonstrating that the fitting exercise is ill-posed even when making simplifying assumptions to reduce the number of fitting parameters.

To a posteriori test whether the $V\theta/D_{RS} \ll 1$ approximation is appropriate, we can first rewrite it as follows:

$$\frac{V\theta}{D_{RS}} = \frac{C_1\left(1-\frac{b}{a}\right)(t-t_0)^{1-\frac{b}{a}}}{D_{RS}} \quad (19)$$

As noted previously, because $C_1 > 0$ for $b < a$ and $C_1 < 0$ for $b >$ a, C1(1−(b/a)) is always positive. Therefore, $V\theta/D_{RS}$ will grow over time for $b < a$ and decay over time for $b > a$. As such, $V\theta/D_{RS} \ll 1$ will become increasingly true for a velocity-weakening interface, such as the bare PMMA interface. We have also computed $V\theta/D_{RS}$ for the V inferred from our observations and for a typical value of $D_{RS} \sim 10$ μm, we find $V\theta/D_{RS}$ drops to below 0.2 after 10 min and below 0.1 after 50 min (Extended Data Fig. 6). Note that it is not necessary to have small $V\theta/D_{RS}$ from the beginning. As soon as the approximation is true, we find θ growing with t with some offset t_0 that records the initial process when $V\theta/D_{RS}$ may not necessarily be much smaller than 1.

Data availability

All data used in the analysis are available online at the CaltechDATA repository at https://doi.org/10.22002/jrxvw-23c32. Source data are provided with this paper.

Code availability

VIC-2D software for DIC analysis is commercially available from Correlated Solutions, Inc. Code used to analyse DIC results and to generate figures is available online at the CaltechDATA repository at https://doi.org/10.22002/jrxvw-23c32.

51. Mello, M. Identifying the unique ground motion signatures of supershear earthquakes: theory and experiments. PhD dissertation (California Institute of Technology, 2012).
52. Mello, M., Bhat, H. S., Rosakis, A. J. & Kanamori, H. Identifying the unique ground motion signatures of supershear earthquakes: theory and experiments. *Tectonophysics* **493**, 297–326 (2010).
53. Rubino, V., Rosakis, A. J. & Lapusta, N. Spatiotemporal properties of sub-Rayleigh and supershear ruptures inferred from full-field dynamic imaging of laboratory experiments. *J. Geophys. Res. Solid Earth* **125**, e2019JB018922 (2020).
54. Tal, Y., Rubino, V., Rosakis, A. J. & Lapusta, N. Illuminating the physics of dynamic friction through laboratory earthquakes on thrust faults. *Proc. Natl Acad. Sci. USA* **117**, 21095–21100 (2020).
55. Lattanzi, A. et al. Uncertainty analysis of dynamic rupture measurements obtained through ultrahigh-speed digital image correlation. *Exp. Mech.* **63**, 529–563 (2023).
56. Tullis, T. E. & Weeks, J. D. Constitutive behavior and stability of frictional sliding of granite. *Pure Appl. Geophys.* **124**, 383–414 (1986).
57. Blanpied, M. L., Lockner, D. A. & Byerlee, J. D. Frictional slip of granite at hydrothermal conditions. *J. Geophys. Res.* **100**, 13045–13064 (1995).
58. Marone, C., Raleigh, C. B. & Scholz, C. H. Frictional behavior and constitutive modeling of simulated fault gouge. *J. Geophys. Res.* **95**, 7007–7025 (1990).
59. Segall, P. & Rice, J. R. Dilatancy, compaction, and slip instability of a fluid-infiltrated fault. *J. Geophys. Res.* **100**, 22155–22171 (1995).
60. Hulikal, S., Lapusta, N. & Bhattacharya, K. Static and sliding contact of rough surfaces: effect of asperity-scale properties and long-range elastic interactions. *J. Mech. Phys. Solids* **116**, 217–238 (2018).
61. Dieterich, J. H. & Kilgore, B. D. Direct observation of frictional contacts: new insights for state-dependent properties. *Pure Appl. Geophys.* **143**, 283–302 (1994).
62. Berthoud, P., Baumberger, T., G'Sell, C. & Hiver, J.-M. Physical analysis of the state- and rate-dependent friction law: static friction. *Phys. Rev. B* **59**, 14313–14327 (1999).
63. Ben-David, O., Rubinstein, S. M. & Fineberg, J. Slip-stick and the evolution of frictional strength. *Nature* **463**, 76–79 (2010).
64. Ikari, M. J., Carpenter, B. M. & Marone, C. A microphysical interpretation of rate- and state-dependent friction for fault gouge. *Geochem. Geophys. Geosyst.* **17**, 1660–1677 (2016).
65. Perfettini, H. & Molinari, A. A micromechanical model of rate and state friction: 1. Static and dynamic sliding. *J. Geophys. Res. Solid Earth* **122**, 2590–2637 (2017).
66. Li, Q., Tullis, T. E., Goldsby, D. & Carpick, R. W. Frictional ageing from interfacial bonding and the origins of rate and state friction. *Nature* **480**, 233–236 (2011).
67. Dieterich, J. H. in *Mechanical Behavior of Crustal Rocks: The Handin Volume* Geophysical Monograph Series, Vol. 24 (eds Carter, N. L. et al.) 103–120 (American Geophysical Union, 1981).
68. Stesky, R. M. Rock friction-effect of confining pressure, temperature, and pore pressure. *Pure Appl. Geophys.* **116**, 690–704 (1978).
69. Brechet, Y. & Estrin, Y. The effect of strain rate sensitivity on dynamic friction of metals. *Scr. Metall. Mater.* **30**, 1449–1454 (1994).
70. Chester, F. M. Effects of temperature on friction: constitutive equations and experiments with quartz gouge. *J. Geophys. Res.* **99**, 7247–7261 (1994).
71. Heslot, F., Baumberger, T., Perrin, B., Caroli, B. & Caroli, C. Creep, stick-slip, and dry-friction dynamics: experiments and a heuristic model. *Phys. Rev. E* **49**, 4973–4988 (1994).
72. Sleep, N. H. Application of a unified rate and state friction theory to the mechanics of fault zones with strain localization. *J. Geophys. Res.* **102**, 2875–2895 (1997).
73. Baumberger, T. Contact dynamics and friction at a solid-solid interface: material versus statistical aspects. *Solid State Commun.* **102**, 175–185 (1997).
74. Persson, B. N. J. On the theory of rubber friction. *Surf. Sci.* **401**, 445–454 (1998).
75. Perfettini, H. & Avouac, J.-P. Postseismic relaxation driven by brittle creep: a possible mechanism to reconcile geodetic measurements and the decay rate of aftershocks, application to the Chi-Chi earthquake, Taiwan. *J. Geophys. Res.* **109**, B02304 (2004).

Acknowledgements We thank J.-P. Avouac, M. Acosta, A. Lattanzi and P. Arakalian for their discussions about and help with the experiments; A. Kiani and GALCIT machine shop at Caltech for specimens manufacturing; M. Gori for his involvement with preliminary experiments; and D. Mojahedi for administrative work related to the project. This study is supported by the US National Science Foundation (NSF) (EAR-2045285 and EAR-1651235), the US Geological Survey (grant nos. G20AP00037 and G16AP00106) and the NSF-IUCRC Center for Geomechanics and Mitigation of Geohazards (GMG) at California Institute of Technology (NSF award no. 1822214). Matlab was used to analyse the results and prepare the figures.

Author contributions N.L., A.J.R. and V.R. conceived the study. K.S. and V.R. designed the experiments. K.S. performed the measurements. K.S. and S.L. analysed the data. All authors contributed to interpreting the results and writing the paper.

Competing interest The authors declare no competing interests.

Additional information

Supplementary information The online version contains supplementary material available at https://doi.org/10.1038/s41586-025-08673-0.

Correspondence and requests for materials should be addressed to Krittanon Sirorattanakul.

Peer review information *Nature* thanks Chris Marone and Allan Rubin for their contribution to the peer review of this work. Peer reviewer reports are available.

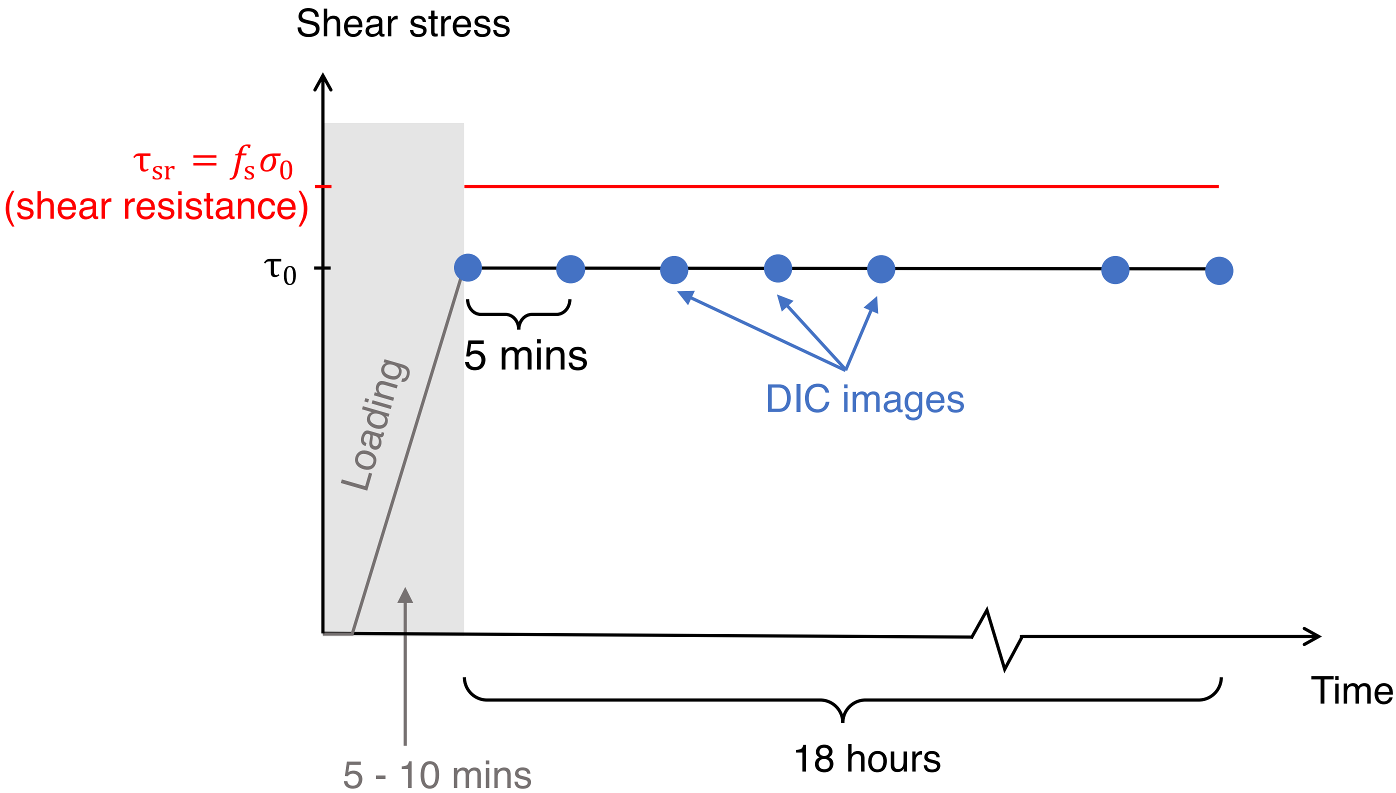

Extended Data Fig. 1 | A schematic summarizing the experimental procedure. For each test, a specimen with an inclination angle α is loaded uniaxially to a preset load $P = 10$ MPa with resolved normal stress $\sigma_0 = P\cos^2\alpha = 8.08$ MPa and resolved shear stress $\tau_0 = P\sin\alpha\cos\alpha = 3.94$ MPa. The load is maintained for 18 h (6.48×10^4 seconds), and optical images are taken every 5 min.

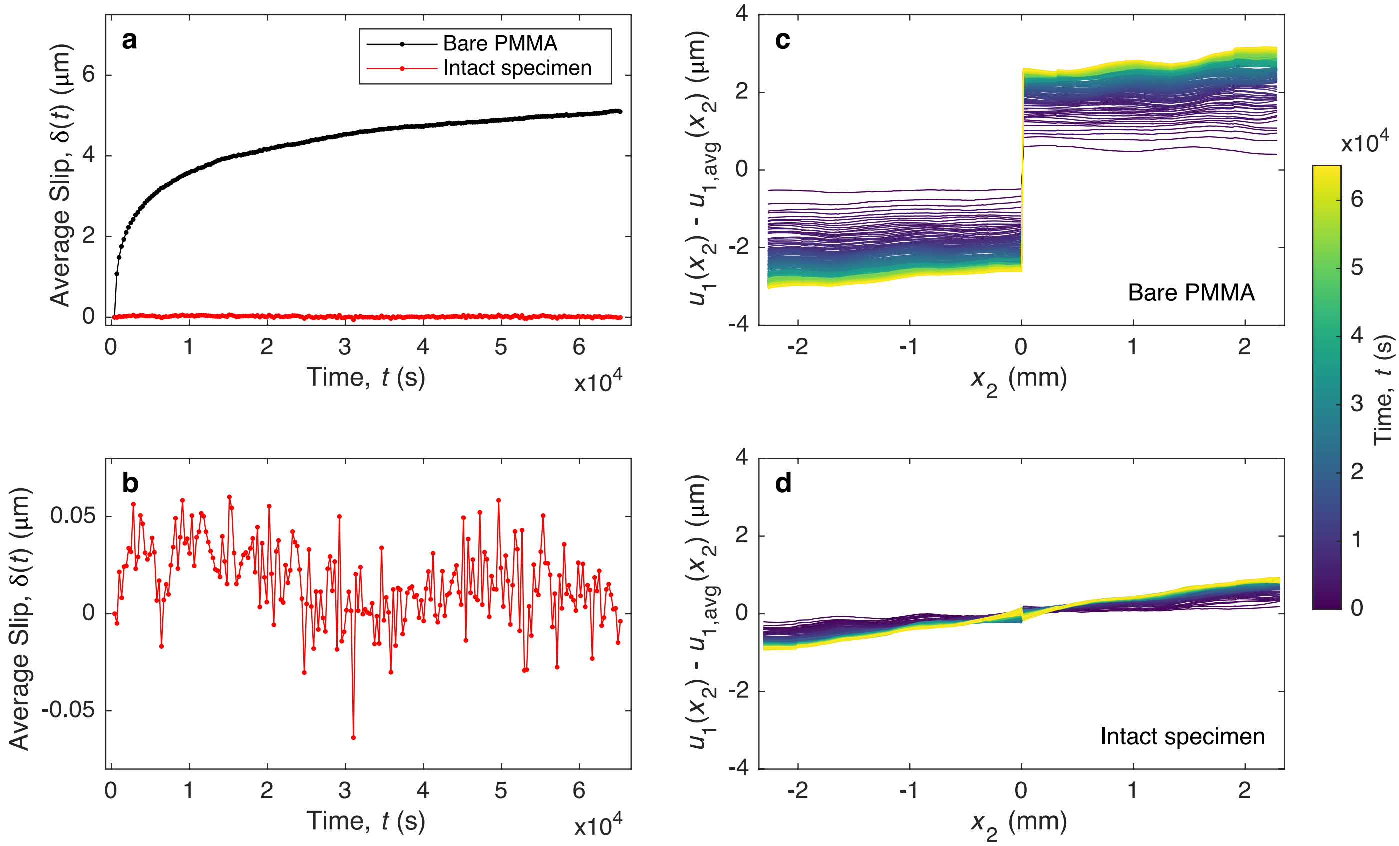

Extended Data Fig. 2 | Comparison of bare PMMA test (with interface) with an intact specimen (no interface). (a) Average accumulated slip $\delta(t)$ measured using identical experimental procedures and data analysis for a specimen with bare PMMA interface and a reference intact specimen without any interface indicating potential bulk effects and/or experimental error. (b) is the zoomed in version of (a). The comparison clearly shows the slip measured along nominally stationary PMMA interfaces is much larger than the experimental error and bulk effects. (c) A representative profile of the measured fault-parallel displacement u_1 across the direction x_2 (perpendicular to the interface) for bare PMMA surface, color coded by time. (d) is similar to (c) but for an intact specimen. The average displacement $u_{1,avg}$ for each profile is subtracted to remove any rigid body translation that may be due to some small vibration of camera or the optical table allowing for better visualization. The profile in (c) looks more like a step function than an S-shape, dismissing shear-induced deformation of material near interface from contributing in any substantial way to the observed accumulated slip $\delta(t)$.

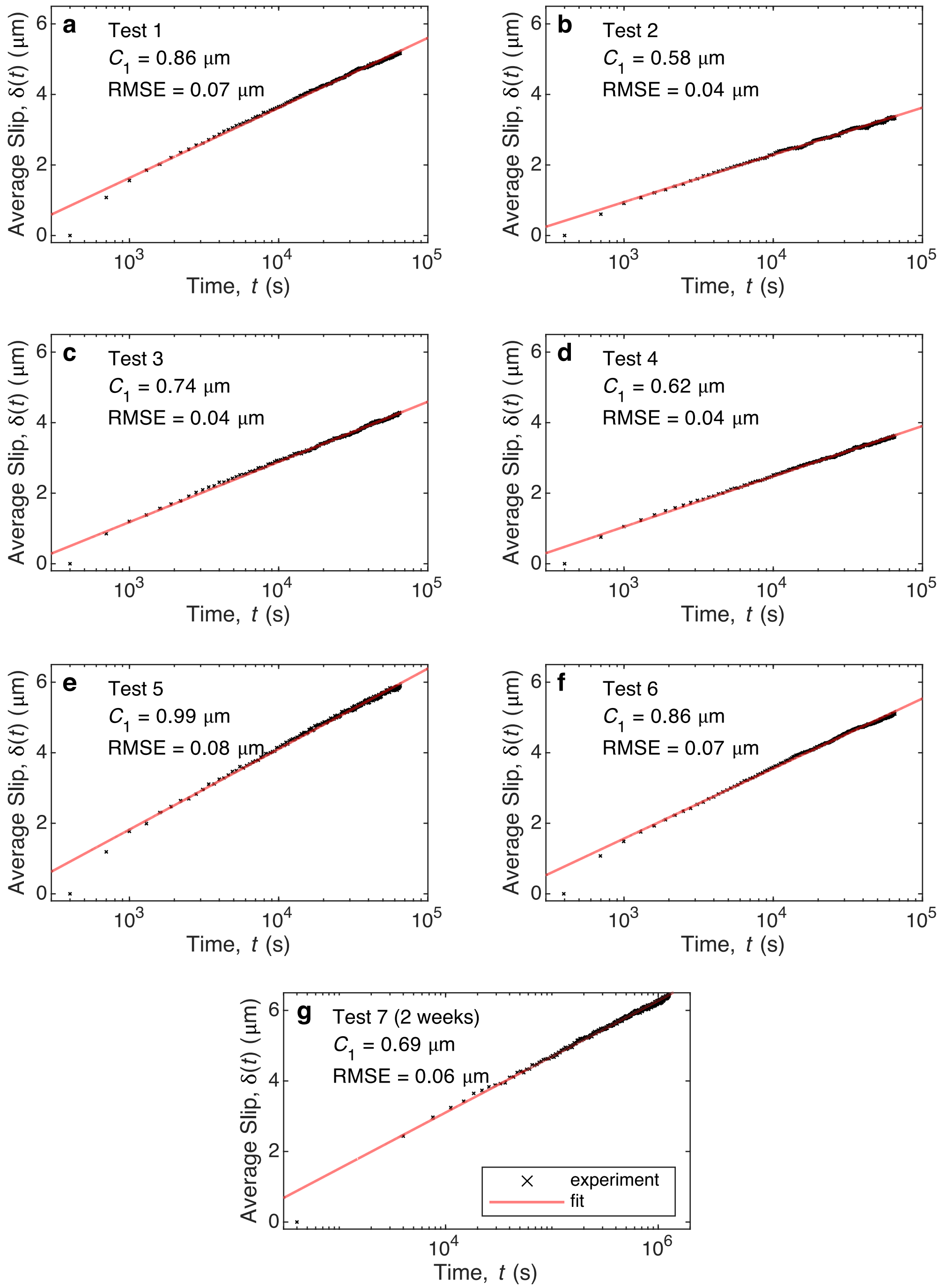

Extended Data Fig. 3 | Explaining the measured accumulated slip on bare PMMA interfaces using logarithmic functions. (a–g) Seven experiments are performed for bare PMMA interfaces. For each individual test, the interfaces are re-polished and re-beadblasted to ensure their repeatability. The bare PMMA tests shown in the main text Fig. 2 are test 1 (18 hr) and test 7 (2 weeks). The experimentally measured accumulated slips are fitted using the logarithmic functions (equation (3), $\delta(t) = C_1 \ln(t + t_0) + C_2$). The results are also compiled in Supplementary Table 1.

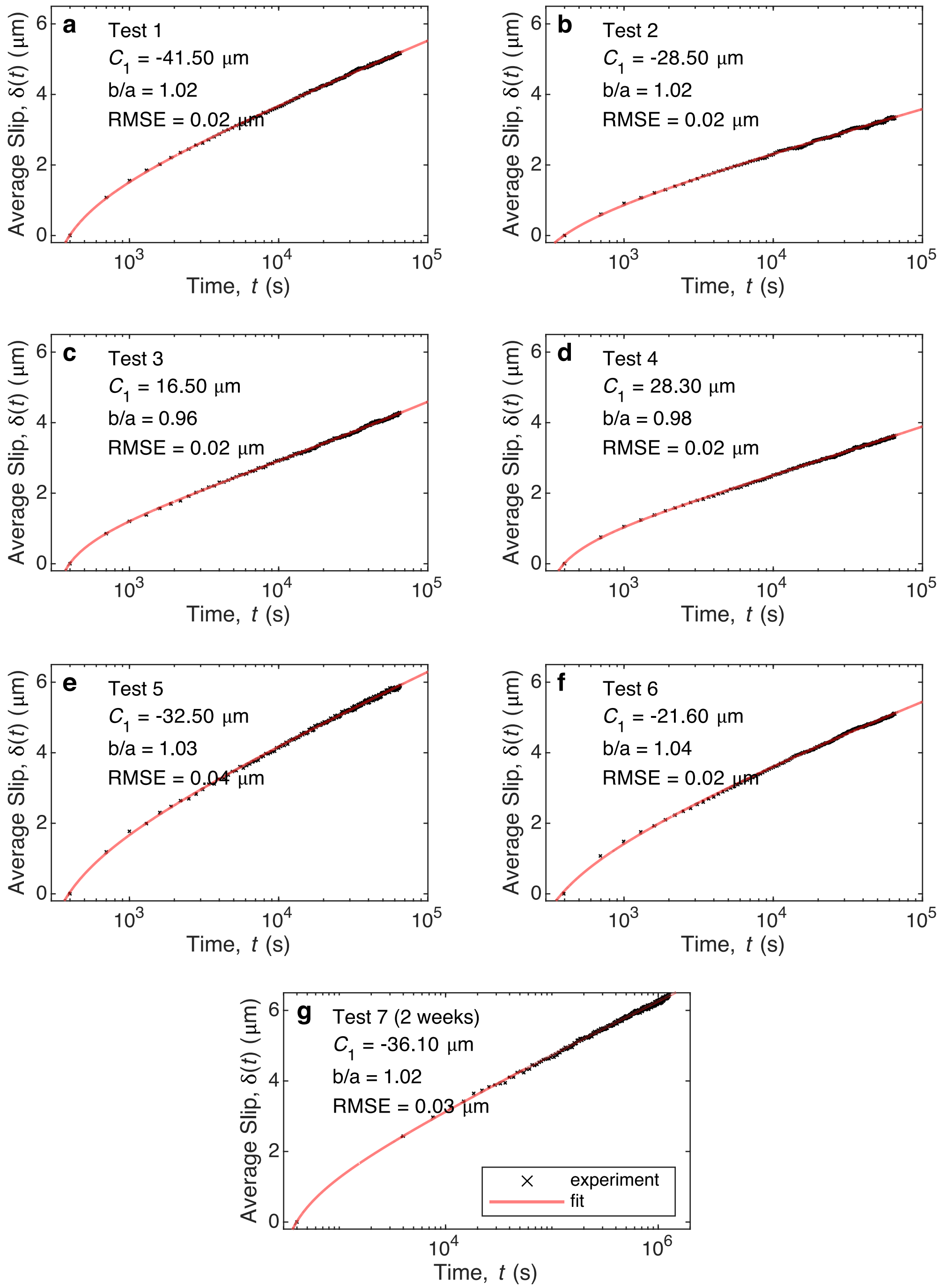

Extended Data Fig. 4 | Explaining the measured accumulated slip on bare PMMA interfaces with power laws. (a–g) Seven experiments are performed for bare PMMA interfaces (same as those shown in Extended Data Fig. 3). The experimentally measured accumulated slips are fitted using the power laws (equation (4), $\delta(t) = C_1(t - t_0)^{1-b/a} + C_2$). The results are also compiled in Supplementary Table 3.

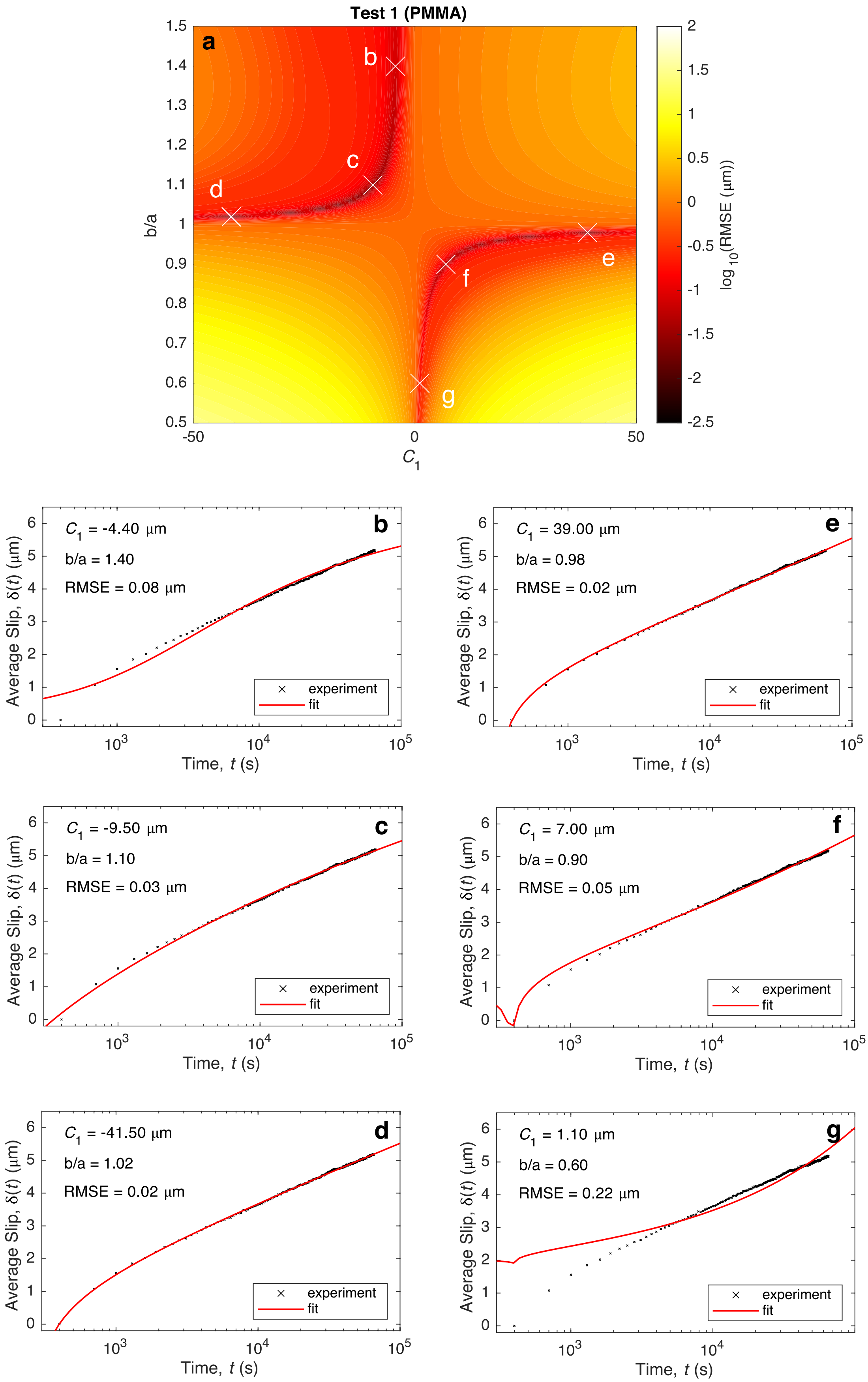

Extended Data Fig. 5 | Evaluating the fitting quality. To demonstrate the sensitivity of the fitting parameters, we evaluate the results from fitting averaged accumulated slip of bare PMMA interfaces with power laws (equation (4), $\delta(t) = C_1(t - t_0)^{1-b/a} + C_2$). (a) Root-mean-square error (RMSE) for the explored parameters space. (b–g) Fitting results are displayed for six sets of parameters that resulted in relatively small RMSE. While there are parameters with velocity-strengthening and velocity-weakening that result in a small RMSE, visual inspection of the fit favors velocity-neutral parameters.

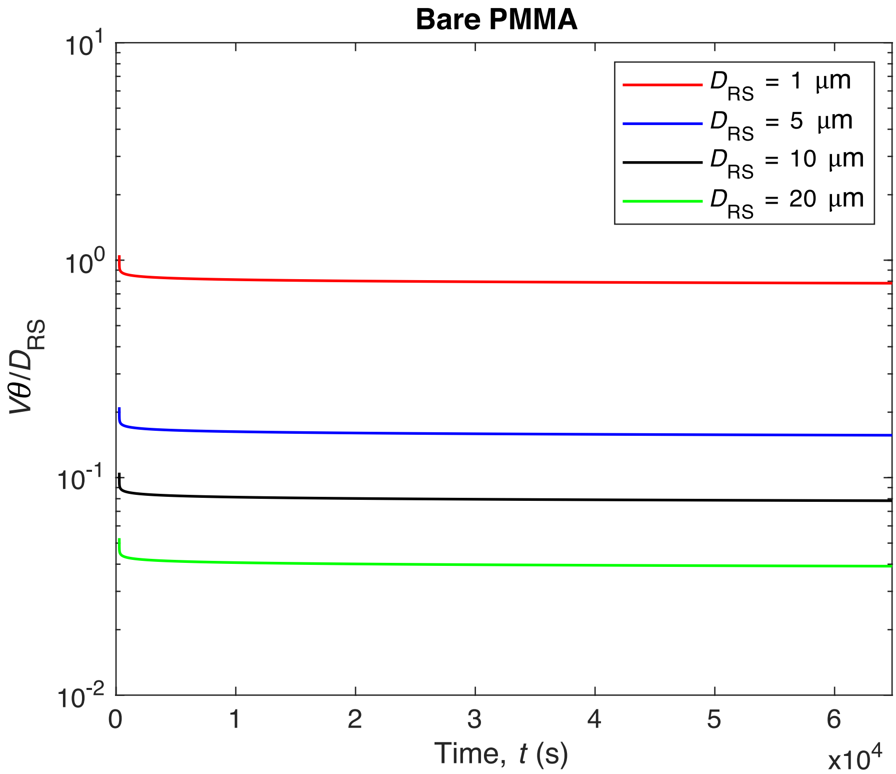

Extended Data Fig. 6 | Evaluating a posterior the $V\theta/D_{RS} \ll 1$ approximation. Calculations of $V\theta/D_{RS}$ using the best-fit V and t_0 from bare PMMA test 1 for different possible values of D_{RS}. For a typical value of $D_{RS} = 10$ µm, $V\theta/D_{RS}$ drops to below 0.1 after 4.5 min.

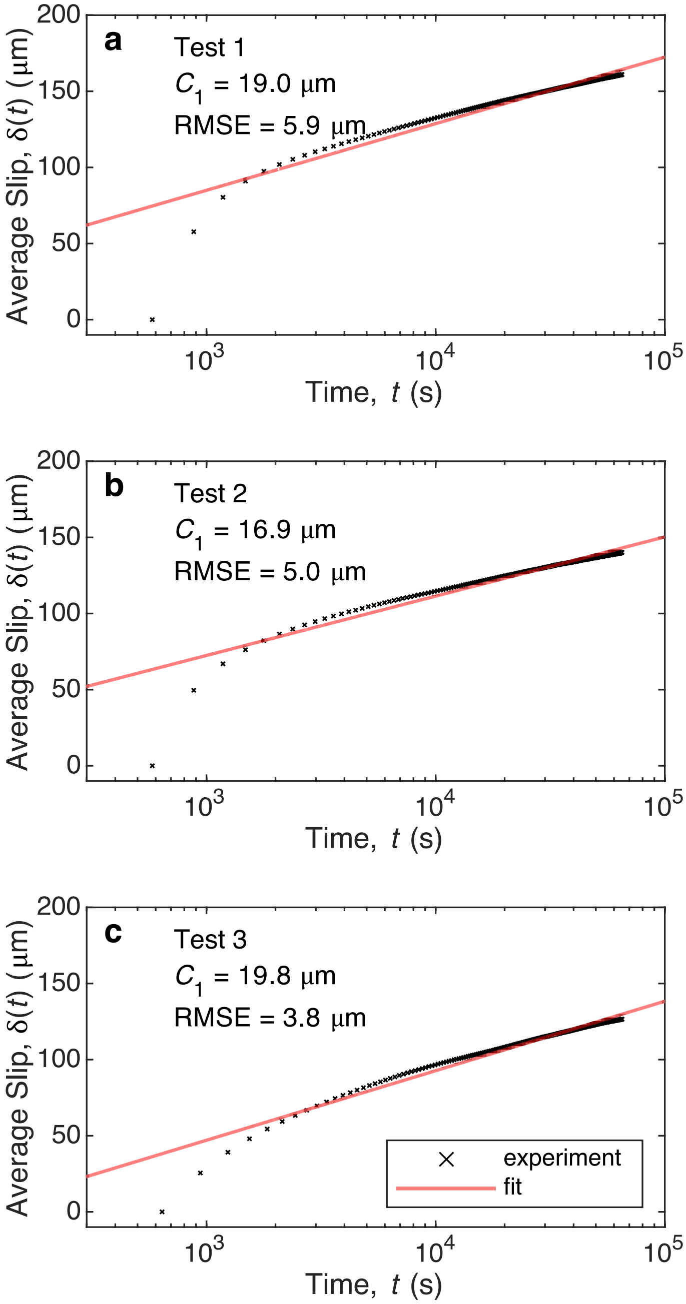

Extended Data Fig. 7 | Explaining the measured accumulated slip on interfaces embedded with rock gouge with logarithmic functions. (a–c) Three experiments are performed for interfaces embedded with rock gouge. For each individual test, the interfaces are re-polished and re-beadblasted, and the gouge layer is re-packed to ensure their repeatability. The gouge test shown in the main text Fig. 3 is test 1 (18 hr). The experimentally measured accumulated slips are fitted using the logarithmic functions (equation (3), $\delta(t) = C_1 \ln(t + t_0) + C_2$). The results are also compiled in Supplementary Table 2.

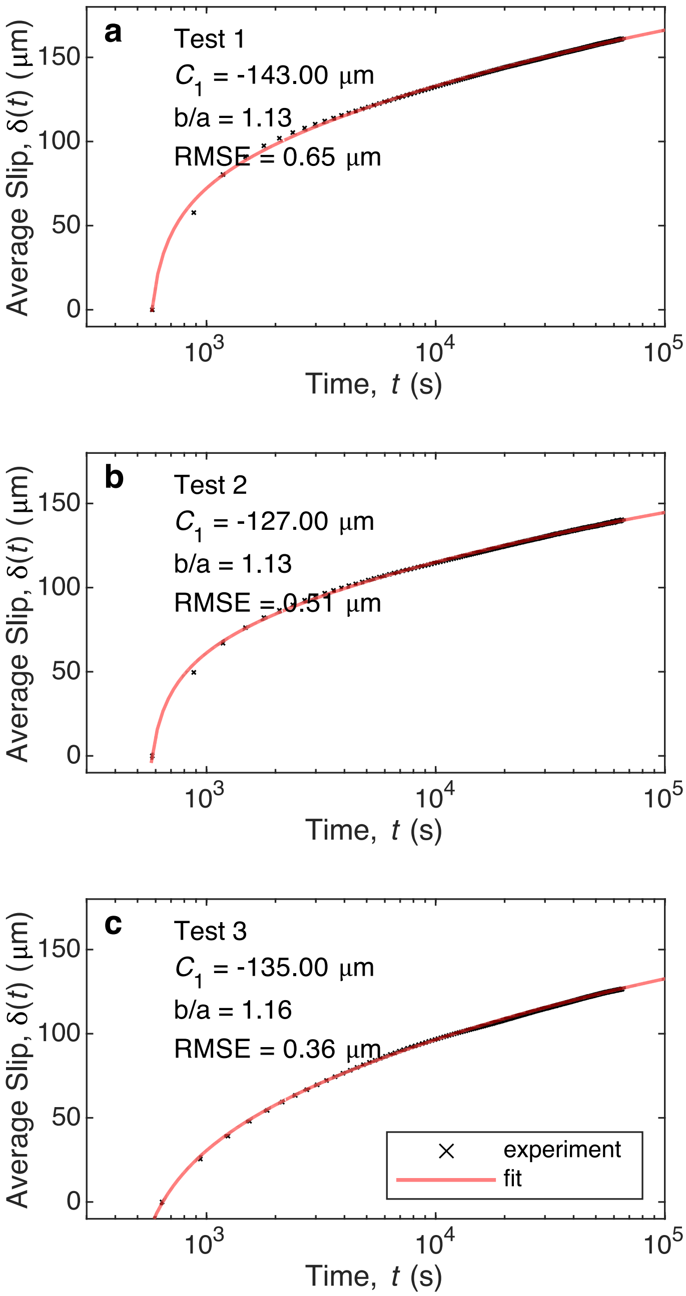

Extended Data Fig. 8 | Explaining the measured accumulated slip on interfaces embedded with rock gouge with power laws. (a–c) Three experiments are performed for interfaces embedded with rock gouge (same as those shown in Extended Data Fig. 7). The experimentally measured accumulated slips are fitted using the power laws (equation (4), $\delta(t) = C_1(t - t_0)^{1-b/a} + C_2$). The results are also compiled in Supplementary Table 4.

Extended Data Table 1 | Digital image correlations (DIC) hardware parameters used in this study

Imaging Parameters	Values
Camera	Imaging Source monochrome camera DMK 37BUX250
Image Size	3 MP, 2048 x 1536 px^2
Lens	Schneider Optics Xenoplan compact series (21-1001976) with 10 mm extension ring
Focal Length	50 mm
Aperture	f/2.8
Field-of-View	30 x 22.5 mm^2
Image Scale	68.3 px/mm
Stand-Off Distance	300 mm
Image Acquisition Rate	32 frames at 50 fps every 5 mins
Exposure Time	0.02 s
Patterning Technique	base coat of Krylon white paint with small black and white speckles on top
Pattern Feature Size	5 px

Extended Data Table 2 | Digital image correlations (DIC) analysis parameters used in this study

DIC Parameters	Values
DIC Software	Correlated Solutions VIC-2D (version 6.2.0)
Image Filtering	32 frames numerically averaging
Reference Image	single reference image (standard correlation)
Interpolant	continuous splines (8-tap)
Matching Criterion	zero-normalized squared differences
Subset / Element Size	41 px (approximately 0.6 mm)
Step Size	1 px (approximately 15 μm)
Subset Shape Function	Affine
Subset Weights	Gaussian